# Inherently Multimodal Nanoparticle-Driven Tracking and Real-Time Delineation of Orthotopic Prostate Tumors and Micrometastases

Tracy W. Liu,[†,‡,§] Thomas D. MacDonald,[†,‡,||] Cheng S. Jin,[‡,||] Joseph M. Gold,[‡,§] Robert G. Bristow,[‡,§,⊥] Brian C. Wilson,[‡,§] and Gang Zheng[‡,§,||,*]

[‡]Ontario Cancer Institute, Campbell Family Institute for Cancer Research and Techna Institute, UHN, 610 University Avenue, Toronto, ON Canada M5G 2M9, [§]Department of Medical Biophysics, University of Toronto, 610 University Avenue, Toronto, ON Canada M5G 2M9, [||]Department of Pharmaceutical Sciences, University of Toronto, 144 College Street, Toronto, ON Canada M5S 3M2, and [⊥]Princess Margaret Cancer Center, UHN, 610 University Avenue, Toronto, ON Canada M5T 2M9. [†]Contributed equally to this work (T.W.L. and T.D.M.).

ABSTRACT Prostate cancer is the most common cancer among men and the second cause of male cancer-related deaths. There are currently three critical needs in prostate cancer imaging to personalize cancer treatment: (1) accurate intraprostatic imaging for multiple foci and extra-capsular extent; (2) monitoring local and systemic treatment response and predicting recurrence; and (3) more sensitive imaging of occult prostate cancer bone metastases. Recently, our lab developed porphysomes, inherently multimodal, all-organic nanoparticles with flexible and robust radiochemistry. Herein, we validate the first *in vivo* application of ^{64}Cu-porphysomes in clinically relevant orthotopic prostate and bony metastatic cancer models. We demonstrate clear multimodal delineation of orthotopic tumors on both the macro- and the microscopic scales (using both PET and fluorescence) and sensitively detected small bony metastases (<2 mm). The unique and multifaceted properties of porphysomes offers a promising all-in-one prostate cancer imaging agent for tumor detection and treatment response/recurrence monitoring using both radionuclide- and photonic-based strategies.
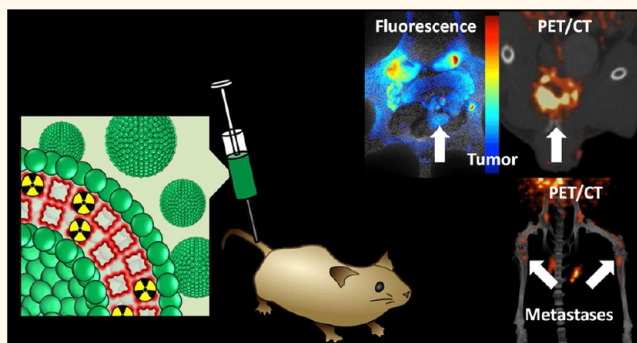
KEYWORDS: orthotopic · prostate cancer · porphysomes

There is a consensus among the medical community that the perfunctory use of radical therapies is leading to the widespread overtreatment of biologically indolent prostate cancers.[1−4] Alternative, nonradical, treatment strategies include active surveillance of indolent cancers and intraprostatic focal therapies (rather than treating the entire gland to preclude or minimize side effects of treatment).[2,5−8] At the other end of the spectrum, for advanced stage disease, there is a great need to triage patients with occult micrometastatic disease to better systemic therapies to cure patients that have minimal systemic burden to decrease prostate cancer-related deaths in men.[9] Imaging plays a critical role in all of these strategies. Therefore, improvements in prostate cancer imaging must include the ability to delineate small areas of multifocal disease and micrometastases in an accurate and precise manner. Anatomical imaging modalities such as MRI, ultrasound, and CT are the most common current imaging methods used to assess prostate cancer. Unfortunately, all three have unsatisfactorily low accuracies in detecting clinically significant disease, as cancerous tissue is often indistinguishable from healthy tissues.[1,10−16] Therefore, to personalize medicine, clinicians have three critical needs for prostate cancer imaging: (1) accurate intraprostatic imaging at early stages; (2) monitoring treatment response and imaging early recurrence; and (3) imaging of prostate cancer bone micrometastases. An imaging modality that could accurately describe the disease in these three states would give clinicians the
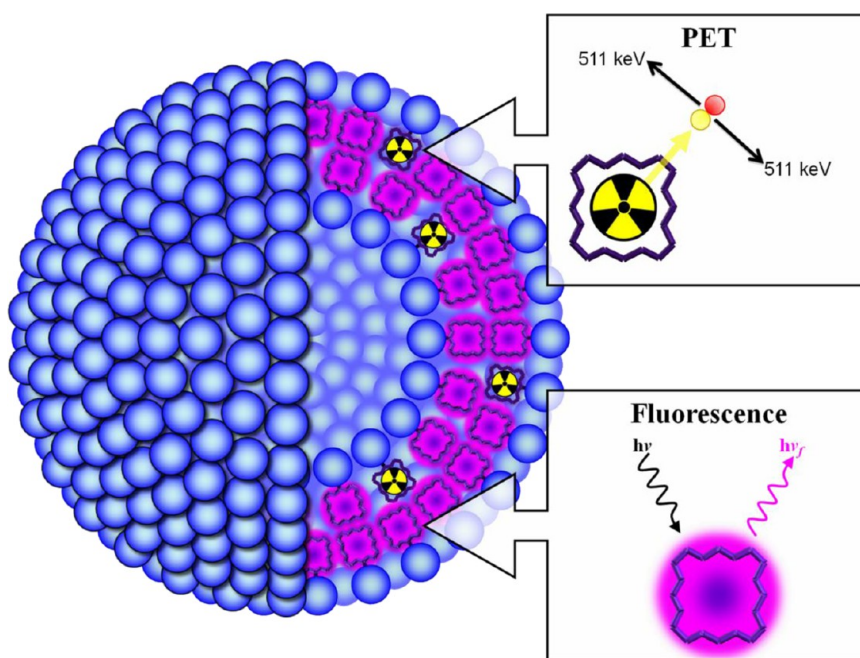
Figure 1. Schematic diagram of the multimodal properties of ^{64}Cu-porphysomes as a result of directly radiolabeling a fraction of the porphyrin−lipid bilayer of preformed photonic porphysomes creating intrinsic multimodal nanoparticles.

information necessary to properly classify disease extent and prognosis and plan treatment based on initial and intratreatment response. Notable among the emerging imaging modalities are functional imaging techniques such as fluorescence imaging and positron emission tomography (PET). Optical imaging has received much attention due to its ease of implementation, operational simplicity, low cost, and ability to provide real-time information about surgical margins, thereby extending the surgeon's vision ensuring complete surgical resection of tumors.[17−20] PET provides quantitative drug biodistribution, effective treatment planning and monitoring and noninvasive deep tissue (>5 cm) images,[21] key characteristics beyond what is achievable by fluorescence imaging.[22,23] With the emergence of multimodal imaging strategies and development of unique contrast agents, the complementary ability of different imaging systems, such as fluorescence and PET/CT, could enable high-resolution and sensitivity in patient assessment.[24−27]

Porphyrins are a unique platform for the development of multifunctional imaging agents. Found in nature, porphyrins are exceptionally strong metal ion chelators with inherent photonic properties.[28] By chelating a positron emitting metal ion such as copper-64 (^{64}Cu) with a porphyrin, one can create a highly stable radiotracer.[29−33] Alas, the paramagnetic nature of copper 2+ ions quenches the porphyrins natural fluorescence, so multiple porphyrins are necessary to create a multifunctional probe. An elegant solution lies in the use of the porphyrin-based nanoparticles, porphysomes.[34] We recently demonstrated that ^{64}Cu can be directly incorporated into a small fraction of the

porphyrin molecules in a porphysome to create a single, simple, all-organic nanostructure that is both PET and fluorescently active (Figure 1).[35]

^{64}Cu-porphysomes, which are self-assembled from a single porphyrin-lipid building block, stand apart from other nanoparticles as they can be radiolabeled directly, without the need for exogenous chelators or other modifications. By including the radionuclide directly into the building blocks, the nanoparticles can be faithfully tracked *in vivo* while ensuring that the pharmacokinetics and biodistribution are not affected.[35] By virtue of being composed of a single, biodegradable building block,[36] ^{64}Cu-porphysomes achieve a high level of multifunctionality while being free of the complexity and toxicity plaguing other multifunctional nanoparticles[37] (i.e., complex multi-component biocompatible nanoparticles (liposomes, polymers), toxic or poorly cleared inorganic-core nanoparticles, *etc.*[24,38−42]). While the unlabeled porphysome scaffold is nontoxic,[34] toxicity could arise from the application of excessive amounts of radioactivity. However, this is easily avoided by controlling the amount of activity per particle with the very flexible labeling procedure.[35] These intrinsically multimodal ^{64}Cu-porphysomes are well suited for prostate cancer imaging given nonindolent, malignant prostate tissue is twice as vascularized as healthy prostate.[43] Thus, we expect increased ^{64}Cu-porphysome uptake and retention in nonindolent prostate tumors owing to the nanoparticle's ability to extravasate through malignant vasculature.[44] Critically, to evaluate ^{64}Cu-porphysome, we have used several clinically relevant prostate cancer models; orthotopic models whereby prostate tumor
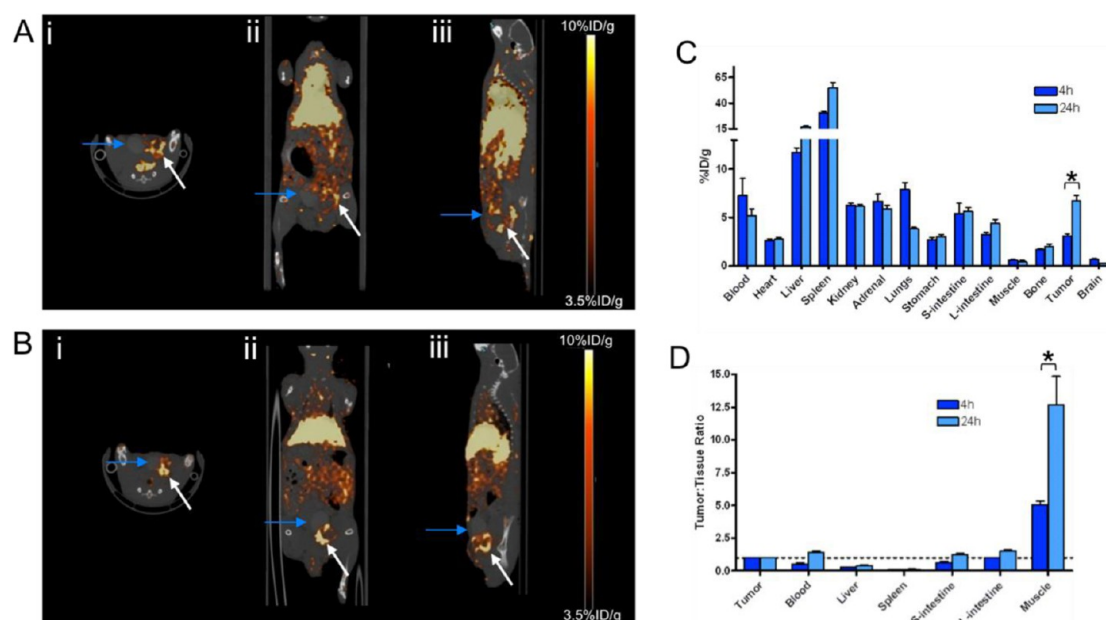
Figure 2. ^{64}Cu-porphysomes uptake studies in orthotopic prostate cancer model. Representative MicroPET/CT images of (i) axial, (ii) coronal, and (iii) sagittal single slices through the orthotopic PC3 tumor at (A) 4 h and (B) 24 h post-*i.v.* injection of 500 μCi ^{64}Cu-porphysomes: white arrows, tumor; blue arrows, bladder; n = 4). (C) Biodistribution of ^{64}Cu-porphysomes at 4 and 24 h post-*i.v.* injection, plotted as % injected dose/gram (%ID/g). (D) Tumor-to-tissue ratio in select tissues at 4 and 24 h. Each point is mean $\pm$ 1 SEM of four determinations (*$p < 0.001$, $n = 4$).

cells are implanted and grown in the prostate gland itself better mimicking the clinical growth, location, and microenvironment of the disease displayed by patients and a systemic metastatic model representing the spread of prostate cancer to the bone.

Herein, we report a proof-of-principle study evaluating this nanoparticle driven platform for multimodality imaging and discuss the clinical potential of ^{64}Cu-porphysomes to address the current clinical needs in prostate cancer imaging. ^{64}Cu-porphysomes accumulate selectively in localized prostate tumors with low nonspecific accumulation in surrounding healthy prostate, allowing for clear tumor delineation. We then show ^{64}Cu-porphysomes' ability to sensitively detect small (<2 mm) prostate-derived bony metastases. The ^{64}Cu-porphysome platform has potential for detecting disease progression, treatment planning, and monitoring treatment response and recurrence. To the best of our knowledge, this is the first report of a multimodal PET and fluorescent nanoparticle delineating prostate tumors and micrometastases.

RESULTS

^{64}Cu-Porphysome Uptake in the PC3 Orthotopic Tumor Model. The tumor uptake of ^{64}Cu-porphysomes was evaluated in the PC3 orthotopic model at 4 and 24 h postintravenous injection. Time points beyond two half-lives of ^{64}Cu were not investigated, as this would require both high radioactivity doses and long scan times to achieve measurable activity. At 4 h, the prostate tumor was not easily delineated in the PET/CT image (Figure 2A) and the radioassay studies demonstrated a tumor %ID/g of only 3.16 $\pm$ 0.36 (Figure 2B). The low tumor and high

intestinal uptake (5.50 $\pm$ 2.09%ID/g) gives a low tumor-to-tissue ratio (0.62 $\pm$ 0.18), making it difficult to visualize the tumor at 4 h. In contrast, the tumor is clearly identifiable at 24 h (Figure 2C,D) due to a significant ($p < 0.001$), greater than 2-fold increase in tumor uptake, 6.83 $\pm$ 1.08%ID/g (Figure 2B), increasing the tumor-to-gut ratio to 1.53 $\pm$ 0.28 (Figure 2D). The retention of ^{64}Cu-porphysomes within the tumor is evident from the tumor-to-muscle ratio increasing from 5.06 $\pm$ 0.49 to 12.7 $\pm$ 6.1 from 4 to 24 h (Figure 2D).

Similar to many other nanoparticles, porphysomes are cleared through the hepatobiliary route, resulting in the high accumulation within the liver and spleen.[39,45] Importantly, no accumulation was observed in the bladder at any time point, which has been the "Achilles heel" of many small molecule radiotracers used in prostate cancer imaging given that the normal tissue signal of the bladder overlays with that of the target tissue signal of the prostate gland. The 24 h time point was chosen as the optimum imaging time, as it provides the highest prostate tumor uptake, delineation, and high tumor-to-background ratio.

^{64}Cu-Porphysome Selectivity in Orthotopic Prostate Tumor. We then tested the selectivity of ^{64}Cu-porphysomes within the PC3 and 22RV1 orthotopic prostate cancer models. Figure 3 displays representative PET/CT images comparing the PC3 (Figure 3A) and 22RV1 (Figure 3B) models with healthy male mice (Figure 3C) at 24 h post-^{64}Cu-porphysome intravenous injection.

^{64}Cu-porphysomes clearly delineate the orthotopic tumors, while the non-tumor-bearing mice displayed minimal signal in the prostate region. Encouragingly,
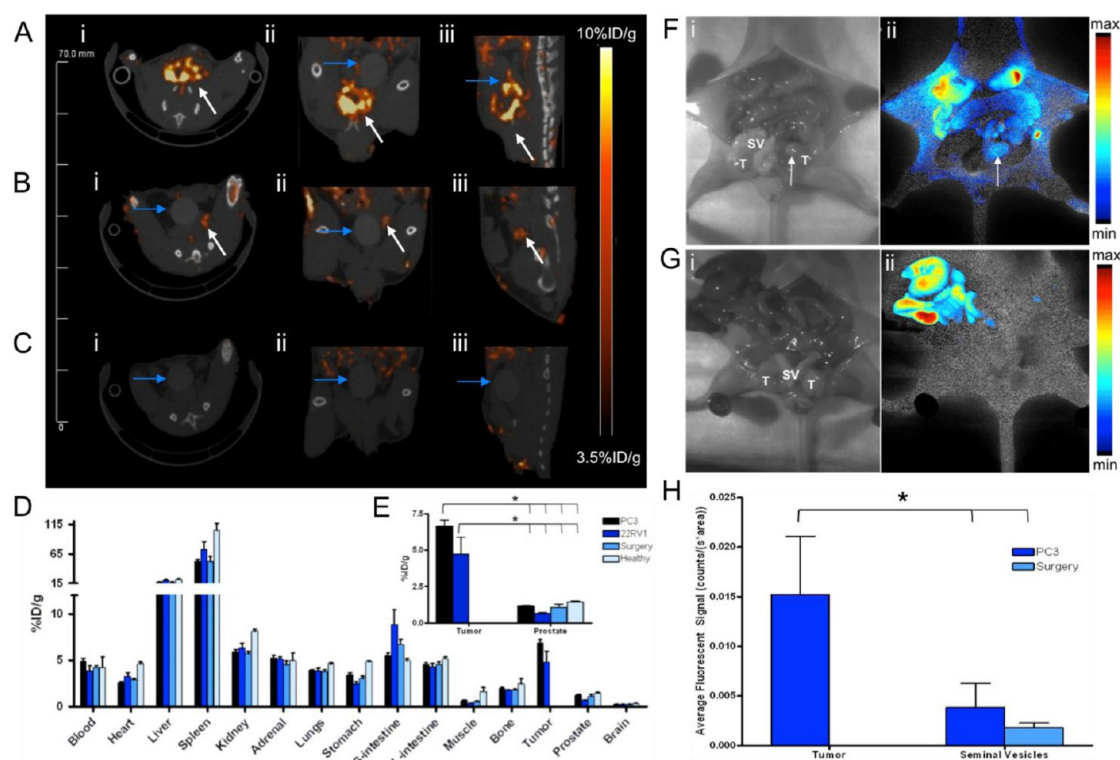
Figure 3. ^{64}Cu-porphysome selectivity in orthotopic prostate tumor models. Representative MicroPET/CT images of (i) axial, (ii) coronal, and (iii) sagittal single slices through (A) orthotopic PC3 tumor ($n = 8$), (B) orthotopic 22RV1 tumor ($n = 3$), and (C) healthy male mice ($n = 3$) at 24 h after *i.v.* injection of 500 μCi ^{64}Cu-porphysomes: PET image integration time 40 min. White arrows depict prostate tumor; blue arrows depict bladder. (D) Corresponding organ biodistribution measured *ex vivo* in orthotopic PC3 ($n = 4$), orthotopic 22RV1 ($n = 3$), orthotopic surgery control ($n = 5$), and healthy male mice ($n = 3$) using radioassay. (E) Magnified view of the tumor and healthy prostate tissue uptake (*$p < 0.05$). (F) Orthotopic PC3 prostate tumor model and (G) surgery-control mice comparing (i) monochrome and (ii) composite fluorescence and monochrome images: SV, seminal vesicles; T, testes; white arrow, orthotopic prostate tumor. (H) Fluorescent signal for orthotopic PC3 and surgery-control mice comparing tumor and seminal vesicles (*$p < 0.01$, $n = 4$).

^{64}Cu-porphysomes clearly demarcate not only the larger PC3 tumors, but also 22RV1 tumors that were less than half their size (5 and 2 mm, respectively, as determined by MRI; Figure S1). Clear tumor delineation was also demonstrated by fluorescence imaging (Figure 3F,G): PC3 tumors had approximately 9- and 4-fold higher fluorescence (total signal/(ms·area)), compared to the normal prostate tissue in both healthy mice and tumor-bearing animals (Figure 3H). The radioassay data confirmed the selectivity of ^{64}Cu-porphysomes for cancerous tissue: PC3 tumor-to-prostate ratio of 5.75 ± 1.53, with $6.83 \pm 1.08\%$ID/g and $1.23 \pm 0.202\%$ID/g, respectively (Figure 3D,E). The findings in the 22RV1 model were similar, with a tumor-to-prostate ratio of 7.24 ± 2.66 with $4.81 \pm 2.06\%$ID/g and $0.668 \pm 0.132\%$ID/g, respectively. At 24 h post-injection, both PC3 and 22RV1 had tumor-to-muscle ratios >12 (Figure S2). A second control group was used to evaluate whether the surgical tumor inoculation procedure affected the accumulation of ^{64}Cu-porphysome in the prostate gland. However, both the untreated control and surgery-only groups had similar ^{64}Cu-porphysome accumulation: $1.45 \pm 0.167\%$ID/g and $1.10 \pm 0.500\%$ID/g (Figure 3F,G). ^{64}Cu-porphysome

uptake in tumors for both models was significantly higher ($p < 0.05$) than healthy prostate tissue in all groups. There was significant uptake in both the spleen and liver in all models, as would be expected for a nanoparticle which is too large to be cleared by the renal system. The tumor selectivity of ^{64}Cu-porphysomes was further demonstrated by fluorescent microscopy of tissue slices, comparing tumor and uninvolved prostate tissue from the orthotopic PC3 and 22RV1 models with healthy prostate from surgery-only mice (Figure 4).

The regions that demonstrated high porphyrin fluorescence corresponded to areas with cancer cell morphology (oversized nuclei, disorganized structure), while uninvolved prostate tissue, characterized by organized glandular structures with small nuclei, showed minimal porphysome fluorescence. There was minimal fluorescence in the surgery-only prostate tissue sections. In summary, the PET/CT images, the biodistribution data, and the *in situ* fluorescence and fluorescence microscopy all clearly demonstrate the selectivity of ^{64}Cu-porphysomes for malignant tissue in these orthotopic prostate cancer models.

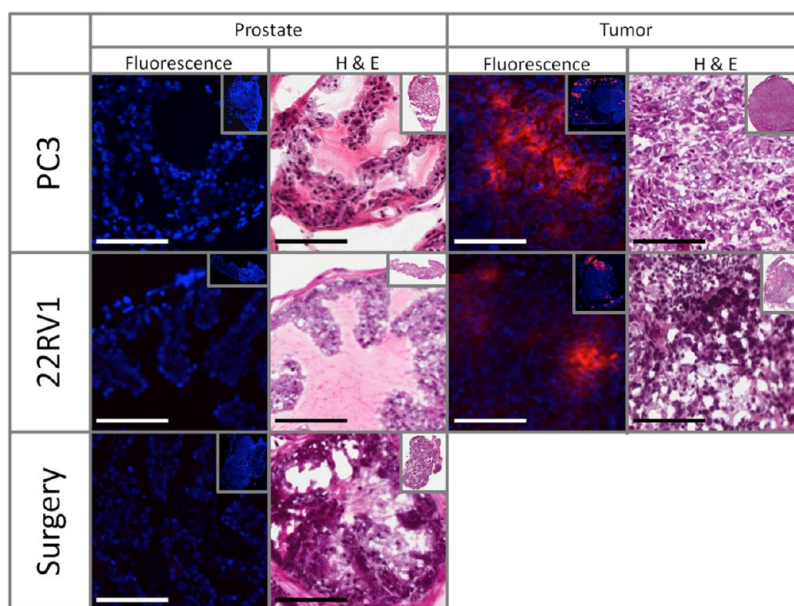**^{64}Cu-Porphysomes for Detection of Metastatic Prostate Tumor.** The metastatic Ace-1-YFP-Luc prostate cancer

Figure 4. Microscopic confirmation of ^{64}Cu-porphysome uptake and selectivity in orthotopic PC3, 22RV1 and surgery-only control groups. Frozen 10 μm tumor and prostate tissue slices were DAPI stained (blue). Representative ^{64}Cu-porphysome fluorescent (red) images were compared to sequential histology slices (H&E staining). Scale bars = 200 μm, whole tissue slice is in the inset (pyro excitation 410 $\pm$ 70 nm, detection 685 $\pm$ 40 nm).

cell line was used to mimic prostate metastases forming in the bone.[46] Metastatic involvement was confirmed in four mice by BLI imaging at 14 d post-Ace-1 injection, as illustrated in Figure 5A, and by post-mortem histology. Healthy control animals demonstrate no bioluminescence (Figure S3). ^{64}Cu-porphysome uptake was seen in the 3D PET/CT images of the corresponding mice at 24 h post-injection (Figure 5Bi), while the healthy animals showed minimal signal in the lower limbs (Figure 5Bii). ^{64}Cu-porphysome accumulation was easily visualized in the lower extremities that were well separated from the high uptake of ^{64}Cu-porphysomes in the liver and spleen. The location of ^{64}Cu-porphysome accumulation in the PET/CT images (Figure 5Bi) matched the localization of metastases in the histology slices; both demonstrate tumors in the distal femur (Figure 5Bi, blue arrow, and Ci) and proximal tibia (Figure 5Bi, white arrow, and Cii,iii). All four mice with confirmed metastases by BLI imaging and histology all demonstrated ^{64}Cu-porphysome accumulation in either the distal femur, proximal tibia, or both. The development of spinal metastases is often associated with prostate cancer. We also evaluated PET/CT imaging of small metastases within the spinal column (Figure 5D,E), confirmed by BLI and H&E histological analysis (Figure 5A,F) in the lumbar vertebrae. There was no corresponding PET signal within the spine in control animals (Figure 5E).

Based on the H&E histology slides (Figure S4), the metastatic lesions ranged from 0.5 to 1.7 mm along the longest axis. Due to the 1.4 mm resolution of the PET imaging system, individual lesions less than 1.4 mm apart were not resolved within the bone by PET. The

uptake of ^{64}Cu-porphysomes was measured from the PET images and demonstrated a mean voxel of 6.40 $\pm$ 0.91, 3.66 $\pm$ 0.30, and 4.11 $\pm$ 0.41%ID/g within metastases found in the spine, femur, and tibia, respectively, with a maximum voxel %ID/g of 9.36 $\pm$ 0.91, 6.36 $\pm$ 0.84, and 7.36 $\pm$ 1.28 (Figure S4). Taken together, the BLI images, the PET/CT images and histology all clearly demonstrate the selectivity of ^{64}Cu-porphysomes to image micrometastases in these metastatic prostate cancer models.

DISCUSSION

One current practice for men presenting with prostate cancer is radical localized treatment, despite the risk and regardless of tumor stage, resulting in significant overtreatment.[2,3] Screening studies suggest that as many as 48 prostate cancer patients need to be treated in order to save one life.[2,3] Radical treatments such as brachytherapy, external beam radiation therapy, and surgery remove or destroy the entire prostate gland in order to ensure complete eradication of the cancer. This approach is often successful at removing disease but drastically decreases patients' quality of life.[47,48] The associated morbidities of radical therapies, primarily impotence and incontinence, are devastating and occur at a high frequency.[47,48] These side effects stem from damage or wholesale removal of neurovascular bundles necessary for normal function. The multifunctional nature of ^{64}Cu-porphysomes may provide a means to avoid these side effects by acting as a PET treatment planning tool, delineating intraglandular foci of prostate tumor involvement, and translating that onto the surgical table or radiotherapy planning through fluorescence image guidance. Beneficially,
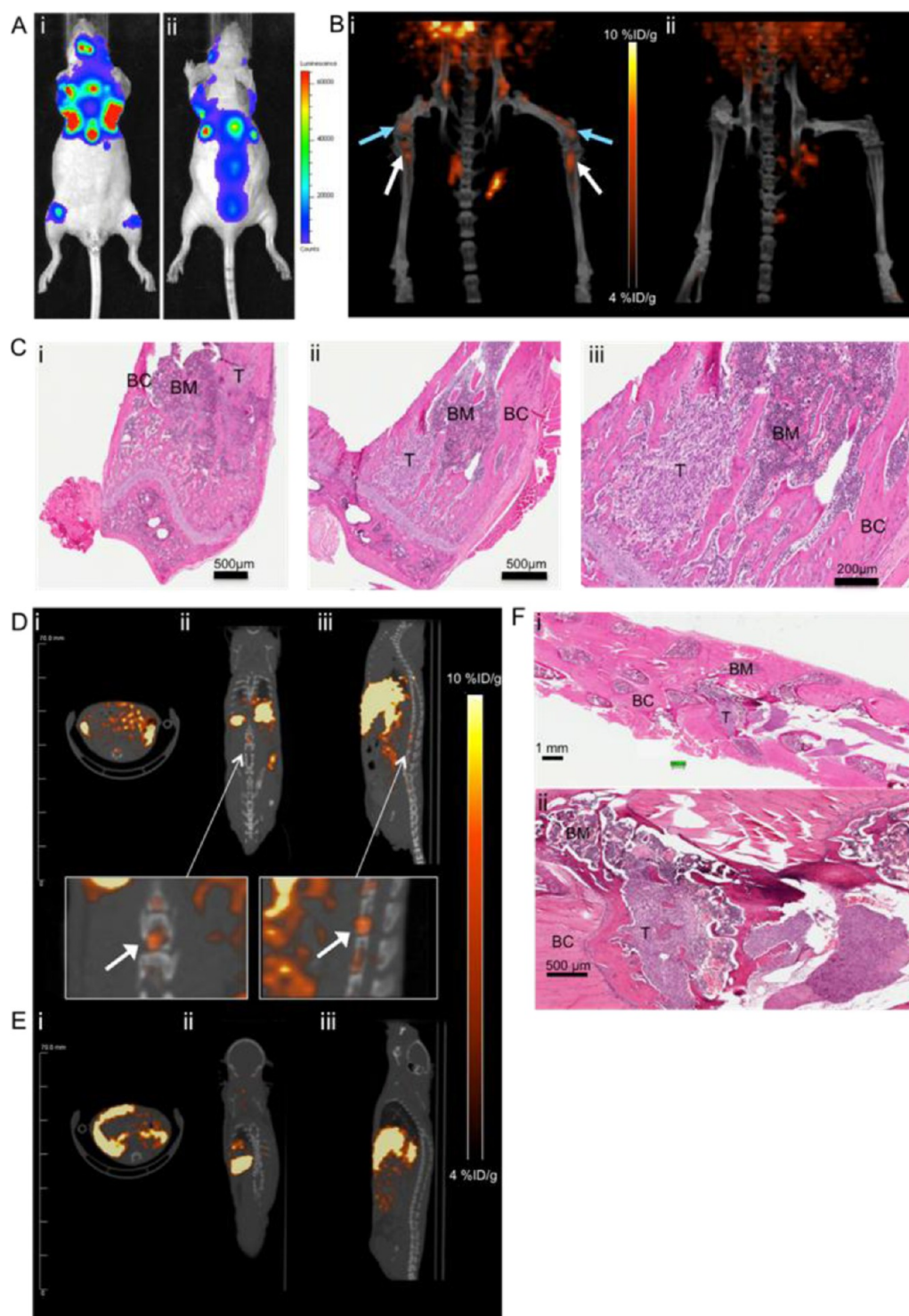
Figure 5. Prostate metastases imaging. (A) Representative bioluminescent images confirming the presence of bony metastases in the supine (i) and prone (ii) positions. **(B)** (i) Corresponding 3D MicroPET/CT images (blue arrow, distal femur metastases; white arrow, proximal tibia metastases) and (ii) 3D MicroPET/CT image of a healthy mouse. **(C)** Corresponding histology (H&E) of lower extremities confirming Ace-1 metastases in the (i) distal femur and (ii, iii) proximal tibia. Representative MicroPET/CT images of (i) axial, (ii) coronal, and (iii) sagittal single slices in **(D)** Ace-1 metastatic and **(E)** control animals 24 h post-*i.v.* injection of 500 μCi ^{64}Cu-porphysomes: inset shows zoomed views of a metastatic lesion. **(F)** Corresponding histology confirming Ace-1 metastases in the spinal column at 1× (i) and 4× (ii) magnification. T, metastases; BM, bone marrow; BC, cortex.

both of these capabilities are derived from a single functional building block, preserving simplicity and making ^{64}Cu-porphysomes more easily translatable.

Here, we mimic localized primary cancer development and its microenvironment using orthotopic prostate cancer models (PC3 and 22RV1). Because

orthotopic tumors are located as they would be clinically, orthotopic models are superior to xenografts for imaging evaluation, as they are not situated in areas of artificially low background signal and so better represent clinical presentation. Similar to other nanoparticles, ^{64}Cu-porphysomes are cleared through the hepatobiliary system, producing minimal background in the bladder and peri-prostatic tissues and allowing clear visualization of the tumor. PET/CT imaging showed that ^{64}Cu-porphysomes delineated hypoxic orthotopic tumors less than 2 mm in size (Figures 2, 3, and S1). *In situ* fluorescence imaging after opening the peritoneal cavity clearly distinguished prostate tumors from the male reproductive organs (healthy prostate, seminal vesicles, and testes), all of which showed minimal fluorescence (Figure 3). Porphysome accumulation was heterogeneous in tumor tissue (seen in both PET/CT and fluorescence), possibly due to high interstitial pressures and the natural heterogeneity of the tumor microenvironment. The exact mechanism of ^{64}Cu-porphysome uptake into cancer *in vivo* is not well understood and is the basis of ongoing studies. It is possible that nanoparticle extravasation drives the tumor accumulation, while the cell penetration capability of the pyropheophorbide-α[49,50] moiety drives the nanoparticle dissociation and cellular uptake. However, this "ringing" effect could be advantageous as it causes the highest uptake to be in the periphery of the tumor, giving a clear indication of the tumor boundaries. ^{64}Cu-porphysomes are able to discriminate between tumor and healthy tissues using both PET/CT and fluorescence imaging modalities.

There are also a number of focal modalities currently under investigation including image-guided focal photothermal therapy, photodynamic therapy, high intensity focused ultrasound ablation, focal brachytherapy, image-guided radiotherapy, and focal cryotherapy.[2] Focal therapies have demonstrated their effectiveness to treat prostate cancer, from indolent to aggressive, with minimal side effects.[1] While attractive due to their low side effects, focal therapies are currently constrained by inadequate tools for accurate intraprostatic imaging. For planning proper disease management, clinicians require a means that accurately depicts the extent of cancer within a diseased prostate. While MRI and trans-rectal ultrasound currently have extensive use in the clinic, they are hampered by limitations such as low sensitivity (particularly for small lesions), low specificity, and irreproducibility.[1,10−16] The PET/CT imaging capability of ^{64}Cu-porphysomes may provide a more accurate picture of tumor involvement within the prostate providing a potential effective treatment planning tool. Treatment planning with ^{64}Cu-porphysome PET/CT imaging not only provides a full picture of the prostate but also is noninvasive and would avert the need for inconvenient, inaccurate, and painful repeated biopsies.[11,51] Additionally, the fluorescence capability of ^{64}Cu-porphysomes and its prostate tumor selectivity provides a means to guide and monitor the efficacy of focal treatment in real time ensuring complete eradication of compromised tissue. Although there is considerable uptake in surrounding nonreproductive tissues (i.e., intestines, Figure 3), in the clinical setting, the field of view for intraoperative imaging[19,52] can be limited to the reproductive organs, where the specificity for tumor over reproductive tissue is the critical parameter.

Assessing a patient's response to treatment is a critical part of tailoring a treatment plan to their needs. Currently there is no method for monitoring response in real-time during a treatment procedure. Fluorescence imaging is an attractive modality for real-time intraoperative monitoring of treatment response as it is highly sensitive and easily implemented. Using orthotopic prostate cancer models, we demonstrated the ability of fluorescent imaging to macroscopically discriminate between diseased and healthy tissue (Figure 3F−H). On the microscopic scale, fluorescence imaging of prostate and tumor tissue histology slices also demonstrated clear separation between tissue types (Figure 4). Porphysome fluorescence only accumulated in malignant cells, confirmed by H&E staining, whereas healthy glandular prostate tissue demonstrated little to no fluorescence. The capability to visually identify malignant cells microscopically using ^{64}Cu-porphysomes could make surgical procedures more successful as surgeons could monitor treatment response in real time, ensuring that the surgical bed is free of any residual tumor cells. This selectivity and the ability to directly visualize diseased tissue with fluorescence may give surgeons the information needed to make nonradical or nerve sparing surgeries more viable.

Currently, the recurrence rate for prostate cancer is as high as 30%.[53] Although, PSA is a valuable biochemical tool for monitoring recurrence after radical therapy,[54] this assay does not give any information with regards to the progression or localization of disease. Patients with rising levels of PSA are again faced in the same unpleasant predicament when prostate cancer was first diagnosed suffering through painful biopsies and the uncertainty of poorly defined disease. There is currently no consensus on effective strategies to monitor and characterize recurrence.[55] Furthermore, the translation of focal therapies into the clinic is constrained by our lack of tools to accurately detect recurrence as healthy prostate tissue spared by focal therapies can confound the PSA assay. The ability of ^{64}Cu-porphysomes to detect prostate tumors less than 2 mm in size by PET/CT (Figure 3 and S1) may present a viable option for identifying tumor foci and detecting the early stages of recurrence noninvasively. The added information demonstrating not only the presence but also the localization of the recurrent
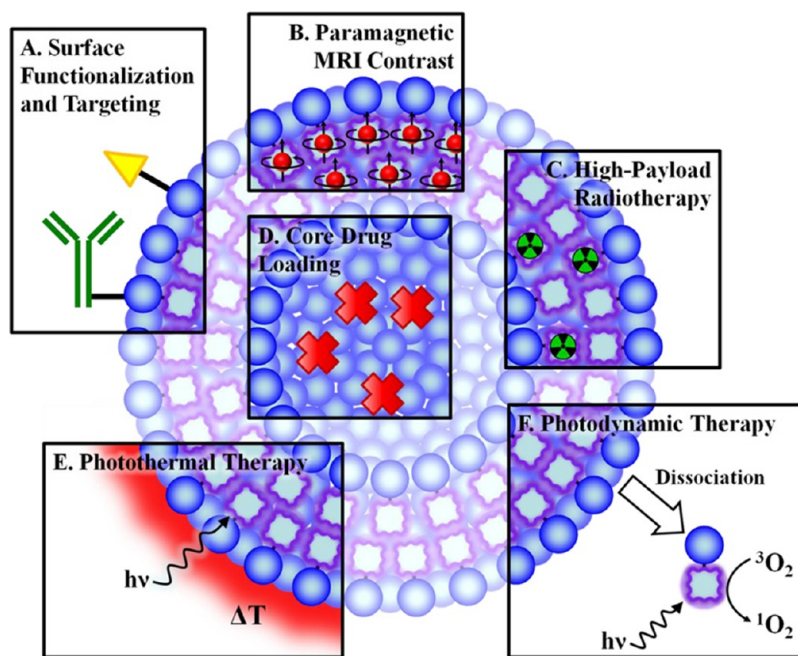
Figure 6. Future potential of porphysomes: (A) targeting the nanoparticles by functionalizing with receptor ligands, antibodies, *etc.*, (B) chelating paramagnetic metal ions with the porphyrin building-blocks for MRI contrast, (C) exploiting porphysomes high-payload chelating abilities to deliver radiotherapeutics, and (D) entrapping soluble drugs or contrast agents within the aqueous core and exploiting the strong absorbance of porphyrins for (E) photothermal therapy with highly quenched, intact porphysomes, and (F) photodynamic therapy with porphyrin-lipid monomers following dissociation of the nanostructure.

tumor may provide clinicians with more information allowing them to better decide upon a treatment regime while giving them the tools needed to bring focal therapies to the forefront of patient care.

Castrate-resistant metastatic spread is associated with death within 18−36 months.[56−59] Currently, there is no ideal strategy for detecting prostate cancer metastases,[60] the primary cause of morbidity and mortality in these patients. A critical clinical need in prostate cancer imaging is the detection of occult metastatic involvement such that systemic agents can be given earlier in the disease spectrum for a more curative approach. Here, we have demonstrated that ^{64}Cu-porphysomes are able to detect >2 mm metastases in the bones of the lower extremities and spinal column in our Ace-1 metastatic cancer model (Figures 5 and S4). Metastases were clearly visualized with PET/CT and confirmed with histological staining. Detection of small metastases has proven difficult for contemporary bone scans which have a detection limit of approximately 1 cm.[61−63] Detecting the metastatic spread to lymph nodes is also of particular interest. We are pursuing the potential of using ^{64}Cu-porphysomes to detect and assess the metastatic involvement of the lymphatic system supported by promising preliminary data of ^{64}Cu-porphysome PET/CT signals (Figure S5). An imaging study including fluorescence-guided surgical resection and histopathological examination of lymph nodes is underway. The dual PET and optical imaging capabilities of ^{64}Cu-porphysomes may be a promising tool for lymph node management as it allows for the noninvasive detection of cancer positive lymph nodes and has application for image-guided assistance intraoperatively. The whole-body imaging capability of PET/CT, combined with the sensitivity of ^{64}Cu-porphysomes to detect small metastatic lesions, 2 mm or smaller, potentially provides a novel and potent means to detect micrometastases, localize metastatic spread, and to monitor local or systemic treatment responses.

These preliminary findings are extremely encouraging but there are limitations to address and more capabilities to explore (Figure 6). ^{64}Cu-porphysomes rely on passive targeting, a phenomenon whose clinical relevance is a point of contention as it does not allow uniform delivery of nanoparticles to all regions of tumors in sufficient quantities. However, as a PEG-coated nanoparticle, the porphysome platform can easily be functionalized with targeting ligands,[34,64] for targets such as PSMA,[65,66] EpCAM,[67] or VEGFR.[68] This functionalization may provide a means to better stratify patients based upon molecular markers, thus personalizing cancer care. Targeting or modifying to PEG shell may also provide a means to reduce ^{64}Cu-porphysomes' high liver and spleen accumulation, thereby improving pharmacokinetics and tumor uptake. Targeted porphysome studies are currently underway. By customizing the porphysome building blocks with a range of porphyrinoids, adding PDT and PTT[34,69] (free-base Pyro or bactheriochlorophyll-a[70]), radio-(immuno)therapy ([67]Cu-porphyrin or ^{177}Lu-texaphyrin),

or MRI (Mn-porphyrin or Gd-texaphyrin) capabilities to porphysomes is easily done. This intrinsic multimodality and flexibility of the porphysome platform lends itself to a broad array of future applications.

CONCLUSIONS

We believe that the porphysome platform has the potential to address several unmet clinical needs in prostate cancer imaging and treatment. The plethora of therapeutic potentials of porphysomes will be enriched by the multimodal imaging properties of ^{64}Cu-porphysomes enabling treatment planning, image-guided therapy, and follow-up monitoring in prostate cancer patients. In conclusion, we have validated the *in vivo* sensitivity and selectivity of ^{64}Cu-porphysomes in a number of clinically relevant prostate cancer models using PET and fluorescence imaging. The unique combination of properties of porphysomes offers a promising all-in-one agent that spans tumor detection, treatment, interventional guidance, treatment response assessment, and monitoring of recurrence, using both radionuclide- and photonic-based strategies.

MATERIALS AND METHODS

Formation of Porphysomes. Porphysomes were synthesized using a previously reported protocol[34] and comprise 65 mol % pyropheophorbide-α-lipid, 30 mol % cholesterol oleate, and 5 mol % DSPE-PEG$_{2000}$. The nanoparticle size was determined by dynamic light scattering (DLS, Malvern Instruments, Malvern, U.K.) and the concentration by UV/vis spectrophotometry (Varian Inc., Palo Alto, CA). The size (z-average) was between 120 and 130 nm with a PDI of <0.2 (Figure S6).

Radiolabeling. ^{64}Cu(OAc)$_2$ was obtained from Université de Sherbrooke, QC, Canada and ^{64}CuCl$_2$ was obtained from Washington University, MO, U.S.A. Porphysomes in PBS were diluted 1:1 with 0.1 M NH$_4$OAC (pH 5.5), before adding a small volume of aqueous ^{64}CuX$_2$ (X = OAc, Cl) solution and incubating at 60 °C for 30 min. Radiochemical purity and yield were assessed on a radio-UPLC (Waters, Milford, MA, U.S.A.) equipped with a UV/vis module (monitoring 254 nm and 410 nm), eSatin radiation detector, and ELSD module using a size exclusion column (pore size 100 nm, mobile phase H$_2$O). ^{64}Cu-porphysomes elute from the size-exclusion column early, while any unchelated ^{64}CuX$_2$ would elute later with the buffer salts and is easily identified in the ELSD channel. The labeled solution was then diluted with PBS to the desired concentration for injection.

Animal Studies. All animal studies were carried out under institutional approval (Ontario Cancer Institute, UHN, Toronto, Canada).

Orthotopic Prostate Tumor Model. Adult male mice (athymic nude, Charles River, 7−8 weeks, 20−25 g average weight) were placed under general anesthesia with 2% isoflurane in oxygen. A small incision was made in the lower abdomen into the peritoneum and the bladder, seminal vesicles, and prostate were partially removed from the abdominal cavity to expose the dorsal prostate lobe. Two different prostate tumor cell lines were used: luciferase-tranfected PC3-luc+ (ATCC, Manassas, VA) and 22RV1 (courtesy Drs. Yoni Pinthus and Robert Bristow). A total of 1.5×10^4 cells in 10 μL of EMEM media or the same volume of cell-free PBS (control) were injected in the dorsal prostate lobe using a 30 G needle. The organs were then returned into the body cavity, the muscle wall and skin were closed with a running 5−0 silk suture, and 0.05 mg/kg buprenorphine and saline solution (0.5 mL) were administered subcutaneously for analgesia. All surgical procedures were carried out under aseptic and pathogen-free conditions in a biosafety hood. Tumor growth was monitored by MRI (Biospec 70/30 USR: Bruker, MA, U.S.A.) at 14 days post-inoculation. PC3 growth was also monitored by bioluminescent imaging (Xenogen, Caliper Life Sciences, MA, U.S.A.) every 7 days.

Metastatic Prostate Cancer Model. All tumor induction procedures were carried out under general anesthesia induced with 4% isoflurane in oxygen (2 L/min) and maintained with 2% isoflurane in oxygen. Ace-1-YFP-Luc cells were kindly provided by Dr. Thomas Rosol (Department of Veterinary Biosciences, College of Veterinary Medicine, The Ohio State University, Columbus, OH 43210). Following the method of Leroy et al.,[46] 10^5 cells were suspended in 100 μL of PBS and injected into the left ventricle of adult male athymic nude mice using a 27 G needle. Saline solution (0.3 mL) and 0.05 mg/kg buprenorphine were then administered subcutaneously and the analgesic was repeated 24 h later. At 14 d post-injection, bioluminescent imaging was performed to assess the development and location of metastatic lesions.

PET/CT Scanning. PET imaging was carried out on a small-animal MicroPET system (Focus 220: Siemens, Munich, Germany). CT imaging was conducted on a microCT system (Locus Ultra: GE Healthcare, U.K.). After tail vein injection of ^{64}Cu-porphysome solution (100−150 uL, 0.43−0.62 mCi, 150−200 nmol pyro-lipid), the mice were imaged under anesthesia (2% isoflurane in oxygen at 2L/min) at 4 or 24 h post-injection, with the images integrated over 10 or 40 min, respectively, followed immediately by CT imaging.

Fluorescence Imaging of Orthotopic Prostate Tumor Models. Immediately after PET/CT imaging at 24 h post-^{64}Cu-porphysome injection, animals were euthanized by cervical dislocation, and fluorescent imaging was performed *in situ* after opening the peritoneal cavity (Maestro: Caliper Life Sciences, MA, U.S.A.) with 680 nm excitation and ≥700 nm detection (autoexposure integration time). Unfortunately, due to the deep-seated nature of orthotopic prostate tumors, *in vivo* fluorescent imaging was unable to detect tumor fluorescence transdermally. Monochrome images were also taken to aid in locating the fluorescence signals. Regions of interest (ROI) were drawn on the monochrome images in which the seminar vesicles, testes and orthotopic prostate tumor were easily distinguishable (Figure S7). These ROIs were then registered onto the fluorescent composite images (images were normalized to background signal) to evaluate the fluorescence from ^{64}Cu-porphysome accumulation in the selected tissues. Comparison of the surgery-only controls with the orthotopic tumor-bearing animals was made on the basis of the total fluorescence signals normalized by exposure time and ROI area (total fluorescent signal/(ms·area)) using a Student t test with a level of significance set at $p < 0.05$. Comparison between different organs in the tumor-bearing animals was made using a paired Student t test with a level of significance set at $p < 0.05$.

Biodistribution. The ^{64}Cu-porphysome biodistribution was determined using the orthotopic PC3 model. At 4 ($n = 4$) or 24 h ($n = 4$) following tail vein injection of ^{64}Cu-porphysome solution (100−150 uL, 0.43−0.62 mCi, 150−200 nmol pyro-lipid), the animals were euthanized using 2% isoflurane and exsanguinated, and the thoracic cavity was opened. Blood samples were withdrawn from the heart. Organs were excised, washed with saline, dried with absorbent tissue, weighed, and counted on a gamma-counter. Organs of interest included the tumor, heart, spleen, lungs, liver, kidneys, adrenal, stomach, small intestine, large intestine, muscle, bone, and brain. The uptake in each uptake was calculated as a percentage of the injected dose per gram of tissue (%ID/g). Comparing 4 and 24 h imaging, pharmacokinetic, and radioassay data, a 24 h time point demonstrated superior tumor uptake and delineation and higher signal-to-background ratio with favorable clearance profile. Additional biodistribution studies were carried out in four separate groups: PC3 orthotopic tumor ($n = 4$), 22RV1

orthotopic tumor ($n = 3$), surgery-only controls ($n = 5$), and non-tumor-bearing/nonsurgical controls ($n = 3$). At 24 h post-tail-vein injection of ^{64}Cu-porphysome solution (100−150 μL, 16−23 MBq, 150−200 nmol pyro-lipid), the mice were euthanized and organs excised as above. The tissues examined also included prostate tumor and healthy prostate in addition to the above organs.

Fluorescence Microscopy and Histology. A single tumor and healthy prostate sample was removed from each of the orthotopic animals (PC3 ($n = 8$) and 22RV1 ($n = 3$) of both tumor and healthy prostate) and control animals (surgery-only control ($n = 5$), non-tumor-bearing/nonsurgical control ($n = 3$) of prostate). All these samples were placed in OCT media, allowed to radioactively decay at −80 °C for 10 half-lives (5 days) and then cryosectioned (six sequential 10 μm sections). Frozen tissue slices (10 μm) were immersed in PBS for 5 min, dried, and then the nuclei were stained using 10 μL of mounting solution with DAPI, 40,6-diamidino-2-phenylindole (Vector Laboratories Inc., CA, U.S.A.). The sections were coverslipped and imaged on a wide-field fluorescence microscope (BX50, Olympus Corporation, PA, U.S.A.) with excitation at 410 ± 70 nm and detection at 685 ± 40 nm. Adjacent sections were H&E stained to confirm tumor. In the Ace-1 metastatic model, the spine, right and left femurs, and tibias were excised and fixed in 10% buffered formalin for one week to allow radioactive decay. The samples were then decalcified using ethylenediaminetetraacetic acid (EDTA, Sigma Aldrich, MO, U.S.A.) for 2 weeks, sectioned (10 μm), and H&E stained to confirm the presence of metastatic lesions within the bone.

Conflict of Interest: The authors declare no competing financial interest.

Supporting Information Available: Supplemental figures are provided. This material is available free of charge *via* the Internet at http://pubs.acs.org.

REFERENCES AND NOTES

1. Ward, J. F., 3rd; Rewcastle, J. C.; Ukimura, O.; Gill, I. S. Focal Therapy for the Treatment of Localized Prostate Cancer: A Potential Therapeutic Paradigm Shift Awaiting Better Imaging. *Curr. Opin. Urol.* **2012**, *22*, 104–108.
2. Lindner, U.; Trachtenberg, J.; Lawrentschuk, N. Focal Therapy in Prostate Cancer: Modalities, Findings and Future Considerations. *Nat. Rev. Urol.* **2010**, *7*, 562–571.
3. Schroder, F. H.; Hugosson, J.; Roobol, M. J.; Tammela, T. L.; Ciatto, S.; Nelen, V.; Kwiatkowski, M.; Lujan, M.; Lilja, H.; Zappa, M.; et al. Screening and Prostate-Cancer Mortality in a Randomized European Study. *N. Engl. J. Med.* **2009**, *360*, 1320–1328.
4. Hoffman, R. M. Screening for Prostate Cancer. *N. Engl. J. Med.* **2011**, *365*, 2013–2019.
5. Bahn, D. K.; Silverman, P.; Lee, F., Sr.; Badalament, R.; Bahn, E. D.; Rewcastle, J. C. Focal Prostate Cryoablation: Initial Results Show Cancer Control and Potency Preservation. *J. Endourol.* **2006**, *20*, 688–692.
6. Ahmed, H. U.; Freeman, A.; Kirkham, A.; Sahu, M.; Scott, R.; Allen, C.; Van der Meulen, J.; Emberton, M. Focal Therapy for Localized Prostate Cancer: A Phase I/II Trial. *J. Urol.* **2011**, *185*, 1246–1254.
7. Lindner, U.; Weersink, R. A.; Haider, M. A.; Gertner, M. R.; Davidson, S. R.; Atri, M.; Wilson, B. C.; Fenster, A.; Trachtenberg, J. Image Guided Photothermal Focal Therapy for Localized Prostate Cancer: Phase I Trial. *J. Urol.* **2009**, *182*, 1371–1377.
8. Lindner, U.; Lawrentschuk, N.; Schatloff, O.; Trachtenberg, J.; Lindner, A. Evolution from Active Surveillance to Focal Therapy in the Management of Prostate Cancer. *Future Oncol.* **2011**, *7*, 775–787.
9. Jemal, A.; Siegel, R.; Ward, E.; Hao, Y.; Xu, J.; Thun, M. J. Cancer Statistics, 2009. *CA Cancer J. Clin.* **2009**, *59*, 225–249.
10. Cooperberg, M. R.; Carroll, P. R.; Klotz, L. Active Surveillance for Prostate Cancer: Progress and Promise. *J. Clin. Oncol.* **2011**, *29*, 3669–3676.
11. Turkbey, B.; Pinto, P. A.; Choyke, P. L. Imaging Techniques for Prostate Cancer: Implications for Focal Therapy. *Nat. Rev. Urol.* **2009**, *6*, 191–203.
12. Halpern, E. J.; Frauscher, F.; Rosenberg, M.; Gomella, L. G. Directed Biopsy During Contrast-Enhanced Sonography of the Prostate. *Am. J. Roentgenol.* **2002**, *178*, 915–919.
13. Loch, T.; Leuschner, I.; Genberg, C.; Weichert-Jacobsen, K.; Kuppers, F.; Yfantis, E.; Evans, M.; Tsarev, V.; Stockle, M. Artificial Neural Network Analysis (ANNA) of Prostatic Transrectal Ultrasound. *Prostate* **1999**, *39*, 198–204.
14. Mirowitz, S. A.; Brown, J. J.; Heiken, J. P. Evaluation of the Prostate and Prostatic Carcinoma with Gadolinium-Enhanced Endorectal Coil MR Imaging. *Radiology* **1993**, *186*, 153–157.
15. Gibbs, P.; Tozer, D. J.; Liney, G. P.; Turnbull, L. W. Comparison of Quantitative T2 Mapping and Diffusion-Weighted Imaging in the Normal and Pathologic Prostate. *Magn. Reson. Med.* **2001**, *46*, 1054–1058.
16. Kurhanewicz, J.; Vigneron, D.; Carroll, P.; Coakley, F. Multiparametric Magnetic Resonance Imaging in Prostate Cancer: Present and Future. *Curr. Opin. Urol.* **2008**, *18*, 71–77.
17. Weissleder, R.; Pittet, M. J. Imaging in the Era of Molecular Oncology. *Nature* **2008**, *452*, 580–589.
18. Solomon, M.; Liu, Y.; Berezin, M. Y.; Achilefu, S. Optical Imaging in Cancer Research: Basic Principles, Tumor Detection, and Therapeutic Monitoring. *Med. Prin. Pract.* **2011**, *20*, 397–415.
19. Liu, Y.; Bauer, A. Q.; Akers, W. J.; Sudlow, G.; Liang, K.; Shen, D.; Berezin, M. Y.; Culver, J. P.; Achilefu, S. Hands-Free, Wireless Goggles for Near-Infrared Fluorescence and Real-Time Image-Guided Surgery. *Surgery* **2011**, *149*, 689–698.
20. Liu, Y.; Solomon, M.; Achilefu, S. Perspectives and Potential Applications of Nanomedicine in Breast and Prostate Cancer. *Med. Res. Rev.* **2013**, *33*, 3–32.
21. Vallabhajosula, S. *Molecular Imaging: Radiopharmaceuticals for PET and SPECT*; Springer-Verlag: Berlin; New York, 2009; p xix.
22. Gambhir, S. S. Molecular Imaging of Cancer with Positron Emission Tomography. *Nat. Rev. Cancer* **2002**, *2*, 683–693.
23. Ntziachristos, V.; Ripoll, J.; Wang, L. H. V.; Weissleder, R. Looking and Listening to Light: The Evolution of Whole-Body Photonic Imaging. *Nat. Biotechnol.* **2005**, *23*, 313–320.
24. Louie, A. Multimodality Imaging Probes: Design and Challenges. *Chem. Rev.* **2010**, *110*, 3146–3195.
25. Jokerst, J. V.; Gambhir, S. S. Molecular Imaging with Theranostic Nanoparticles. *Acc. Chem. Res.* **2011**, *44*, 1050–1060.
26. Nystrom, A. M.; Wooley, K. L. The Importance of Chemistry in Creating Well-Defined Nanoscopic Embedded Therapeutics: Devices Capable of the Dual Functions of Imaging and Therapy. *Acc. Chem. Res.* **2011**, *44*, 969–978.
27. Ali, Z.; Abbasi, A. Z.; Zhang, F.; Arosio, P.; Lascialfari, A.; Casula, M. F.; Wenk, A.; Kreyling, W.; Plapper, R.; Seidel, M.; et al. Multifunctional Nanoparticles for Dual Imaging. *Anal. Chem.* **2011**, *83*, 2877–2882.
28. Policard, A. Etudes Sur Les Aspects Offerts Par Des Tumeurs Experimentales Examinees a La Lumiere De Woods. *C. R. Soc. Biol.* **1924**, 91.
29. Firnau, G.; Maass, D.; Wilson, B. C.; Jeeves, W. P. ^{64}Cu Labelling of Hematoporphyrin Derivative for Non-Invasive

In Vivo Measurements of Tumour Uptake. *Prog. Clin. Biol. Res.* **1984**, *170*, 629–636.

30. Wilson, B. C.; Firnau, G.; Jeeves, W. P.; Brown, K. L.; Burns-McCormick, D. M. Chromatographic Analysis and Tissue Distribution of Radiocopper-Labelled Haematoporphyrin Derivatives. *Laser Med. Sci.* **1988**, *3*, 71–80.

31. Bases, R.; Brodie, S. S.; Rubenfeld, S. Attempts at Tumor Localization Using Cu 64-Labeled Copper Porphyrins. *Cancer* **1958**, *11*, 259–263.

32. Wrenn, F. R., Jr.; Good, M. L.; Handler, P. The Use of Positron-Emitting Radioisotopes for the Localization of Brain Tumors. *Science* **1951**, *113*, 525–527.

33. Shi, J.; Liu, T. W.; Chen, J.; Green, D.; Jaffray, D.; Wilson, B. C.; Wang, F.; Zheng, G. Transforming a Targeted Porphyrin Theranostic Agent into a PET Imaging Probe for Cancer. *Theranostics* **2011**, *1*, 363–370.

34. Lovell, J. F.; Jin, C. S.; Huynh, E.; Jin, H.; Kim, C.; Rubinstein, J. L.; Chan, W. C.; Cao, W.; Wang, L. V.; Zheng, G. Porphysome Nanovesicles Generated by Porphyrin Bilayers for Use as Multimodal Biophotonic Contrast Agents. *Nat. Mater.* **2011**, *10*, 324–332.

35. Liu, T. W.; Macdonald, T. D.; Shi, J.; Wilson, B. C.; Zheng, G. Intrinsically Copper^{64}-Labeled Organic Nanoparticles as Radiotracers. *Angew. Chem., Int. Ed.* **2012**, *51*, 13128–13131.

36. Lovell, J. F.; Jin, C. S.; Huynh, E.; Macdonald, T. D.; Cao, W.; Zheng, G. Enzymatic Regioselection for the Synthesis and Biodegradation of Porphysome Nanovesicles. *Angew. Chem., Int. Ed.* **2012**, *51*, 2429–2433.

37. Huynh, E.; Zheng, G. Engineering Multifunctional Nanoparticles: All-in-One *Versus* One-for-All. *Wiley Interdiscip. Rev. Nanomed. Nanobiotechnol.* **2013**, doi: 10.1002/wnan.1217.

38. Biju, V.; Itoh, T.; Anas, A.; Sujith, A.; Ishikawa, M. Semiconductor Quantum Dots and Metal Nanoparticles: Syntheses, Optical Properties, and Biological Applications. *Anal. Bioanal. Chem.* **2008**, *391*, 2469–2495.

39. Longmire, M.; Choyke, P. L.; Kobayashi, H. Clearance Properties of Nano-Sized Particles and Molecules as Imaging Agents: Considerations and Caveats. *Nanomedicine* **2008**, *3*, 703–717.

40. Ballou, B.; Ernst, L. A.; Andreko, S.; Harper, T.; Fitzpatrick, J. A.; Waggoner, A. S.; Bruchez, M. P. Sentinel Lymph Node Imaging Using Quantum Dots in Mouse Tumor Models. *Bioconjugate Chem.* **2007**, *18*, 389–396.

41. Weissleder, R.; Stark, D. D.; Engelstad, B. L.; Bacon, B. R.; Compton, C. C.; White, D. L.; Jacobs, P.; Lewis, J. Superparamagnetic Iron Oxide: Pharmacokinetics and Toxicity. *Am. J. Roentgenol.* **1989**, *152*, 167–173.

42. Wang, S. Y.; Kim, G.; Lee, Y. E. K.; Hah, H. J.; Ethirajan, M.; Pandey, R. K.; Kopelman, R. Multifunctional Biodegradable Polyacrylamide Nanocarriers for Cancer Theranostics-a "See and Treat" Strategy. *ACS Nano* **2012**, *6*, 6843–6851.

43. Bigler, S. A.; Deering, R. E.; Brawer, M. K. Comparison of Microscopic Vascularity in Benign and Malignant Prostate Tissue. *Hum. Pathol.* **1993**, *24*, 220–226.

44. Matsumura, Y.; Maeda, H. A New Concept for Macromolecular Therapeutics in Cancer Chemotherapy: Mechanism of Tumoritropic Accumulation of Proteins and the Antitumor Agent Smancs. *Cancer Res.* **1986**, *46*, 6387–6392.

45. Davis, M. E.; Chen, Z.; Shin, D. M. Nanoparticle Therapeutics: An Emerging Treatment Modality for Cancer. *Nat. Rev. Drug Discovery* **2008**, *7*, 771–782.

46. LeRoy, B. E.; Thudi, N. K.; Nadella, M. V.; Toribio, R. E.; Tannehill-Gregg, S. H.; van Bokhoven, A.; Davis, D.; Corn, S.; Rosol, T. J. New Bone Formation and Osteolysis by a Metastatic, Highly Invasive Canine Prostate Carcinoma Xenograft. *Prostate* **2006**, *66*, 1213–1222.

47. Wei, J. T.; Dunn, R. L.; Sandler, H. M.; McLaughlin, P. W.; Montie, J. E.; Litwin, M. S.; Nyquist, L.; Sanda, M. G. Comprehensive Comparison of Health-Related Quality of Life after Contemporary Therapies for Localized Prostate Cancer. *J. Clin. Oncol.* **2002**, *20*, 557–566.

48. Sanda, M. G.; Dunn, R. L.; Michalski, J.; Sandler, H. M.; Northouse, L.; Hembroff, L.; Lin, X.; Greenfield, T. K.; Litwin, M. S.; Saigal, C. S.; et al. Quality of Life and Satisfaction with Outcome among Prostate-Cancer Survivors. *N. Engl. J. Med* **2008**, *358*, 1250–1261.

49. Ma, B.; Li, G. L.; Kanter, P.; Lamonica, D.; Grossman, Z.; Pandey, R. K. Bifunctional HPPH-N2S2-Tc-99m Conjugates as Tumor Imaging Agents: Synthesis and Biodistribution Studies. *J. Porphyrins Phthalocyanines* **2003**, *7*, 500–507.

50. Liu, T. W.; Akens, M. K.; Chen, J.; Wise-Milestone, L.; Wilson, B. C.; Zheng, G. Imaging of Specific Activation of Photodynamic Molecular Beacons in Breast Cancer Vertebral Metastases. *Bioconjugate Chem.* **2011**, *22*, 1021–1030.

51. Washington, S. L.; Bonham, M.; Whitson, J. M.; Cowan, J. E.; Carroll, P. R. Transrectal Ultrasonography-Guided Biopsy Does Not Reliably Identify Dominant Cancer Location in Men with Low-Risk Prostate Cancer. *BJU Int.* **2011**, *110*, 50–55.

52. van den Berg, N. S.; van Leeuwen, F. W. B.; van der Poel, H. G. Fluorescence Guidance in Urologic Surgery. *Curr. Opin. Urol.* **2012**, *22*, 109–120.

53. Rocco, B.; Cozzi, G.; Spinelli, M. G.; Grasso, A.; Varisco, D.; Coelho, R. F.; Patel, V. R. Current Status of Salvage Robot-Assisted Laparoscopic Prostatectomy for Radiorecurrent Prostate Cancer. *Curr. Urol. Rep.* **2012**, *13*, 195–201.

54. Freedland, S. J. Screening, Risk Assessment, and the Approach to Therapy in Patients with Prostate Cancer. *Cancer* **2011**, *117*, 1123–1135.

55. Rouvière, O.; Vitry, T.; Lyonnet, D. Imaging of Prostate Cancer Local Recurrences: Why and How?. *Eur. Radiol.* **2010**, *20*, 1254–1266.

56. Mundy, G. R. Mechanisms of Bone Metastasis. *Cancer* **1997**, *80*, 1546–1556.

57. Pinski, J.; Dorff, T. B. Prostate Cancer Metastases to Bone: Pathophysiology, Pain Management, and the Promise of Targeted Therapy. *Eur. J. Cancer* **2005**, *41*, 932–940.

58. Eaton, C. L.; Coleman, R. E. Pathophysiology of Bone Metastases from Prostate Cancer and the Role of Bisphosphonates in Treatment. *Cancer Treat. Rev.* **2003**, *29*, 189–198.

59. Abrahamsson, P.-A. Pathophysiology of Bone Metastases in Prostate Cancer. *Eur. Urol. Suppl.* **2004**, *3*, 3–9.

60. Aus, G.; Abbou, C. C.; Bolla, M.; Heidenreich, A.; Schmid, H. P.; Van Poppel, H.; Wolff, J.; Zattoni, F. Eau Guidelines on Prostate Cancer. *Eur. Urol.* **2005**, *48*, 546–551.

61. Rosenthal, D. I. Radiologic Diagnosis of Bone Metastases. *Cancer* **1997**, *80*, 1595–1607.

62. Gosfield, E., 3rd; Alavi, A.; Kneeland, B. Comparison of Radionuclide Bone Scans and Magnetic Resonance Imaging in Detecting Spinal Metastases. *J. Nucl. Med.* **1993**, *34*, 2191–2198.

63. Schmidt, G. P.; Schoenberg, S. O.; Schmid, R.; Stahl, R.; Tiling, R.; Becker, C. R.; Reiser, M. F.; Baur-Melnyk, A. Screening for Bone Metastases: Whole-Body MRI Using a 32-Channel System *Versus* Dual-Modality PET-CT. *Eur. Radiol.* **2007**, *17*, 939–949.

64. Ng, K. K.; Lovell, J. F.; Vedadi, A.; Hajian, T.; Zheng, G. Self-Assembled Porphyrin Nanodiscs with Structure-Dependent Activation for Phototherapy and Photodiagnostic Applications. *ACS Nano* **2013**, doi: 10.1021/nn400418y.

65. Mease, R. C.; Dusich, C. L.; Foss, C. A.; Ravert, H. T.; Dannals, R. F.; Seidel, J.; Prideaux, A.; Fox, J. J.; Sgouros, G.; Kozikowski, A. P.; et al. *N*-[*N*-[(*S*)-1,3-Dicarboxypropyl]carbamoyl]-4-[^{18}F]-fluorobenzyl-L-cysteine, [^{18}F]DCFBC: A New Imaging Probe for Prostate Cancer. *Clin. Cancer Res.* **2008**, *14*, 3036–3043.

66. Banerjee, S. R.; Pullambhatla, M.; Byun, Y.; Nimmagadda, S.; Green, G.; Fox, J. J.; Horti, A.; Mease, R. C.; Pomper, M. G. ^{68}Ga-Labeled Inhibitors of Prostate-Specific Membrane Antigen (PSMA) for Imaging Prostate Cancer. *J. Med. Chem.* **2010**, *53*, 5333–5341.

67. Tavri, S.; Jha, P.; Meier, R.; Henning, T. D.; Muller, T.; Hostetter, D.; Knopp, C.; Johansson, M.; Reinhart, V.; Boddington, S.; et al. Optical Imaging of Cellular Immunotherapy against Prostate Cancer. *Mol. Imaging* **2009**, *8*, 15–26.

68. Zhang, H. ^{64}Cu-1,4,7,10-Tetraazacyclododecane-1,4,7, 10-tetraacetic Acid-Quantum Dot-Vascular Endothelial Growth Factor. *Molecular Imaging and Contrast Agent Database (MICAD)*; National Center for Biotechnology Information: Bethesda MD, **2004**.

69. Jin, C. S.; Lovell, J. F.; Chen, J.; Zheng, G. Ablation of Hypoxic Tumors with Dose-Equivalent Photothermal, but Not Photodynamic, Therapy Using a Nanostructured Porphyrin Assembly. *ACS Nano* **2013**, *7*, 2541–2550.

70. Liu, T. W.; Chen, J.; Burgess, L.; Cao, W.; Shi, J.; Wilson, B. C.; Zheng, G. Multimodal Bacteriochlorophyll Theranostic Agent. *Theranostics* **2011**, *1*, 354–362.